

# A Chip-Scale Transmitter Module for Real-Time Continuous-Variable QKD

IGOR SERVELLO<sup>1,2</sup>, MARTIN HAUER<sup>1</sup>, MORITZ BAIER<sup>1</sup>, EMMERAN SOLLNER<sup>1</sup>, PETER GLEISSNER<sup>1</sup>, SEBASTIAN RANDEL<sup>2</sup>, ULRICH EISMANN<sup>1</sup>, EMANUEL EICHHAMMER<sup>1</sup>, IMRAN KHAN<sup>1,\*</sup>

<sup>1</sup>KEEQuant GmbH, Gebhardtstraße 28, 90762 Fürth, Germany

<sup>2</sup>Institute of Photonics and Quantum Electronics (IPQ), Karlsruhe Institute of Technology (KIT), Karlsruhe, Germany

\*imran.khan@keequant.com

**Abstract:** Continuous-variable quantum key distribution (CV-QKD) enables secure communication over standard telecom infrastructure, yet its scaling is stalled by bulky, discrete optical hardware. We address this bottleneck by demonstrating a real-time CV-QKD system driven by a chip-scale hybrid transmitter built from commercial telecom components. By integrating a micro-optic external-cavity laser with a monolithic photonic integrated IQ modulator, we provide high performance, enabling secret-key generation over 102 km of optical fiber, while reducing the size of the optics by 95%. Moreover, real-time operation overcomes the offline post-processing bottlenecks of experimental setups. This work bridges laboratory demonstrations and field-deployable technology, with a scalable architecture for cost-effective quantum networks.

## 1. Introduction

The recent advances in quantum computing have highlighted significant vulnerabilities in conventional cryptographic methods. Shor’s algorithm [1] enables sufficiently powerful quantum computers to break many asymmetric cryptography schemes, notably RSA (Rivest–Shamir–Adleman) [2] and DH (Diffie–Hellman) [3]. More generally, the security of classical asymmetric cryptography relies on computational hardness assumptions based on current algorithmic theory; consequently, it remains vulnerable to future cryptography breakthroughs that could invalidate these assumptions. Therefore, current and future communications are at risk, as quantum computers or advances in algorithms could enable retroactive attacks on stored encrypted data, that is, “store-now, decrypt-later” attacks.

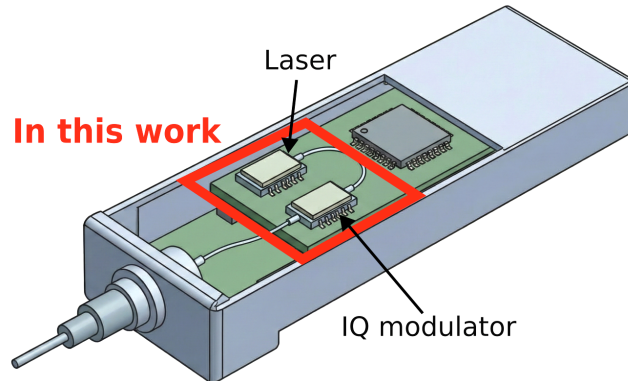


Fig. 1. Concept of a real-time chip-scale CV-QKD transmitter module. This work demonstrates the integration of the optical components of the system (highlighted by the red square) and the automation of the CV-QKD pipeline. *Parts of this figure were generated using the AI-assisted image generation tool Nano Banana.*

Quantum Key Distribution (QKD) is immune against these threats. QKD enables two distant parties to securely establish symmetric cryptographic keys under the assumption of an attacker with infinite (quantum) computational power, enabling true long-term security guaranteed by the principles of quantum mechanics. The first QKD protocol, BB84 [4], exploits the non-orthogonality of two polarization bases and the fundamental behavior of single photons. Following the BB84 protocol, a variety of QKD schemes have been proposed, exploiting different properties of quantum light and detection techniques [5–7]. Among these, Continuous Variable QKD (CV-QKD) has emerged as a particularly promising approach [8].

In CV-QKD, information is encoded on the quadratures of coherent states of light, and the receiver uses coherent detection to measure these quadratures. The security of CV-QKD originates from the non-orthogonality of the quadratures of coherent states. Due to the Heisenberg uncertainty principle, both quadratures cannot be simultaneously measured with arbitrary precision. Any attempt to do so inevitably introduces noise, which enables the detection of eavesdropping and thus allows the implementation of QKD protocols. Because CV-QKD encodes information onto the quadratures of coherent states, it is inherently compatible with standard coherent optical communication systems and can directly leverage their well-established tools and techniques. This compatibility allows the reuse of existing telecom infrastructure, hardware, and digital signal processing (DSP) algorithms, enabling the implementation of high-rate, cost-effective and scalable quantum key distribution systems that can operate alongside conventional optical networks. In this regards, recent works focusing on high symbol rates [9–13], long transmission distances [14–17], and co-propagation of quantum signals with classical telecom channels [18–28], showcase the potential for widespread adoption and practical deployment.

The analogy to classical coherent telecommunications suggests that CV-QKD can follow the same path: miniaturization and cost reduction by means of photonic integrated circuits (PICs). Significant progress has been made towards integrating key components on-chip, including lasers [29], IQ modulators [30], variable optical attenuators (VOAs) [31], balanced detectors [32–34], and combined IQ-modulator/coherent-receiver architectures [35–39]. Despite these advances, the demonstrations to our knowledge have achieved only partially miniaturized modules, as they still rely on essential components based on bulk optics, which prevented the realization of a scalable module. Furthermore, most implementations remain confined to laboratory environments, and rely on offline post-processing, limiting the deployability of the system to real networks.

In this work, we report the first demonstration of a chip-scale CV-QKD transmitter integrating both the light source and modulator. The result is a scalable CV-QKD transmitter module built entirely from telecom-grade, miniaturized components. The QKD system employing the chip-scale transmitter operates in real time, and features fully automated field-deployable operation, achieving real-time key rate generation above 9 kbit/s. The system delivers high performance, with validated key generation up to 102 km of optical fiber links. This work represents a key step from laboratory-scale experiments toward practical, scalable quantum-secure networks.

## 2. Real-time CV-QKD System

This work builds on a CV-QKD system from the *Andariel Testbed Series*, developed by KEEQuant GmbH. The system is composed of two primary blocks: the transmitter (Alice) and the receiver (Bob), which are connected by a single optical fiber. Notably, no additional RF connection e.g. for clock synchronization is needed. The experimental system employed in the study is represented in Fig. 2, with the utilized optical components represented to scale.

In the present implementation, the main discrete optical components on Alice’s side, the laser and the IQ modulator, have been replaced by chip-scale alternatives. The chip-scale components used in this work are shown in Fig. 2, to scale. Compared to the system based on discrete

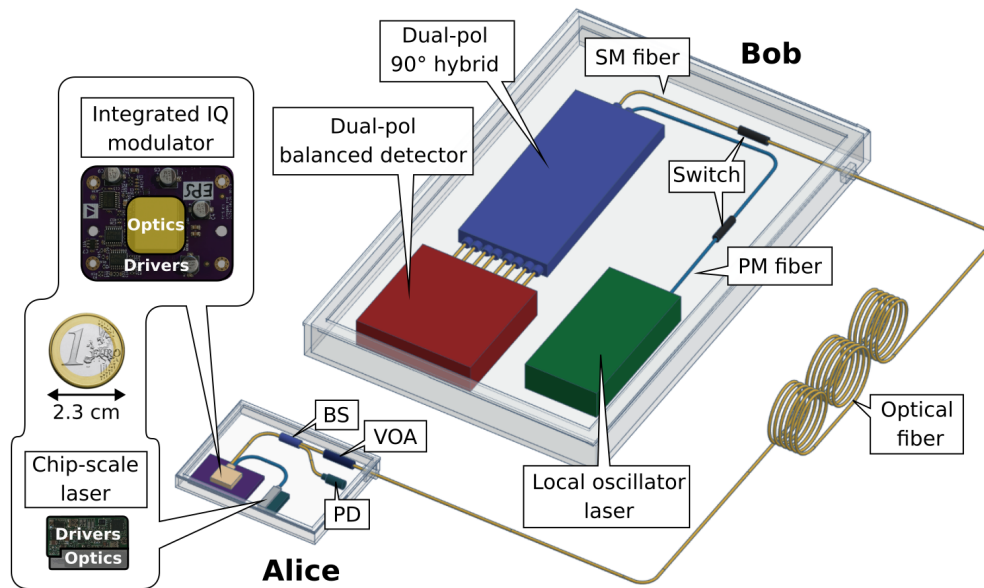


Fig. 2. Schematic of the experimental setup, to scale. The miniaturized CV-QKD transmitter under study (Alice, bottom left) is connected via optical fiber to the receiver (Bob, top right), which is implemented using bulk optical components. On the left hand side are shown photographs (partially obfuscated) of the chip-scale modules used in this work: the IQ modulator and the laser, shown alongside a 1-euro coin for scale.

components, the chip-scale IQ modulator and laser achieve volume reductions by factors of 27 and 23, respectively. Considering the entire transmitter, the miniaturized prototype optical components occupy only 5% of the original volume.

For both nodes, the optical components are interconnected and controlled through dedicated printed circuit boards (PCB). These PCBs host the control electronics, digital-to-analog converters (DACs), analog-to-digital converters (ADCs), and the communication interface with the central processing unit (CPU), providing signal generation, acquisition, and system control.

### 2.1. Transmitter

The transmitter side of the QKD system (Alice) consists of a laser source, an IQ modulator, a VOA, and an optical power meter (PM). The laser generates the coherent optical carrier, which is modulated by the IQ modulator to produce the Gaussian-modulated coherent states required for CV-QKD. The VOA and PM jointly control and monitor the transmitted optical power, thereby setting the desired modulation variance  $V_{\text{mod}}$ .

The laser source is a hybrid micro-integrated external-cavity laser (ECL), comprising an InP gain chip coupled to a micro-optical filter cavity. The schematic of the optical module is represented in Fig. 3. This configuration preserves the high spectral purity and wide tunability required for CV-QKD, which are often compromised in fully monolithic designs. The driving electronics are co-packaged within the module, ensuring compactness and power-efficiency. The laser achieves a linewidth below 28 kHz, provides full tunability across the C-band, and delivers up to 17 dBm of fiber-coupled optical output power.

The IQ modulation is realized using the modulation section of a telecom-grade packaged PIC, represented in Fig. 3. The chip is based on a silicon photonics platform and incorporates a dual-polarization IQ modulator. The PIC features a single fiber-coupled laser input, half

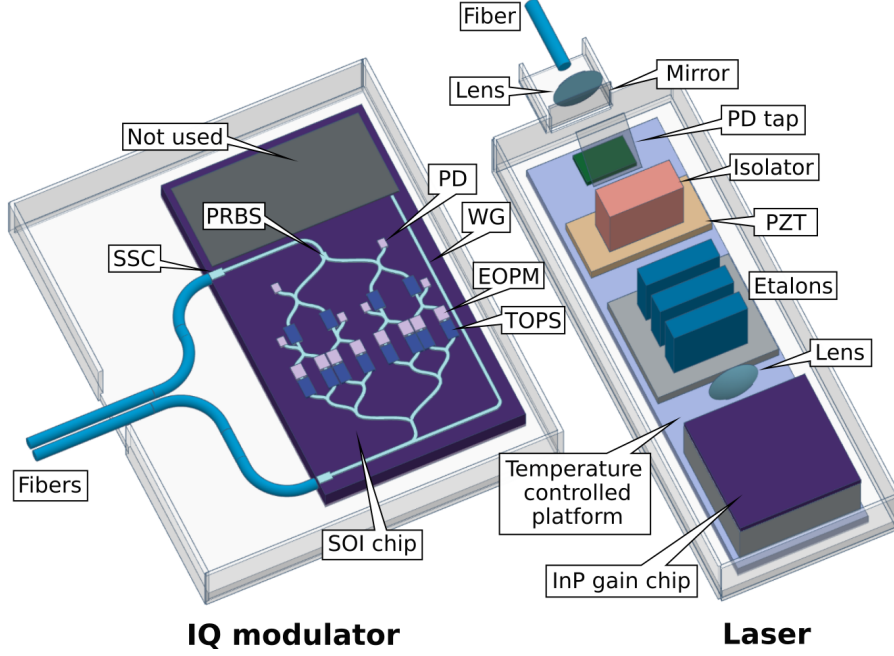


Fig. 3. Illustration of the schematic of the chip-scale modules. On the left, the PIC incorporating the IQ modulator. Only one polarization was modulated in this study. The details of the unused PIC section are not reported. On the right, the chip-scale laser, composed by the InP gain chip and the external cavity. Components are abbreviated as follows: WG: waveguide; PD: photodiode; TOPS: thermo-optic phase shifter; EOPM: electro-optic phase modulator; PRBS: polarization rotator beam splitter; SSC: spot-size converter.

of the input power is directed into the IQ modulator. The optical power is further equally split between the X and Y polarizations. The IQ modulator follows a conventional nested Mach-Zehnder structure, consisting of Mach-Zehnder modulators (MZMs) embedded within a larger Mach-Zehnder interferometer (MZI). All the corresponding phase modulators operate in a push-pull configuration. It provides four RF input ports to drive the electro-optic modulators encoding the quadratures  $I_x$ ,  $Q_x$ ,  $I_y$ , and  $Q_y$ . In the experiments the signal was modulated on a single polarization. Although the system is designed for high symbol rates (up to 70 GBaud), in this work it is driven at a symbol rate of only 156.25 MBaud. Thermal optical phase shifters (TOPS) are included to fine-tune the MZM arms for maximum extinction and to maintain the  $90^\circ$  phase bias between the I and Q branches. The measured half-wave voltage is  $V_\pi = 0.96$  V. Several on-chip monitoring photodiodes are integrated at the outputs of the MZMs and MZIs to facilitate bias control.

**2.2. Receiver**

The receiver side of the system (Bob) currently employs discrete optical components. It consists of a narrow-linewidth tunable laser serving as the LO, a dual-polarization  $90^\circ$  optical hybrid, and a balanced dual-polarization detector with low noise transimpedance amplifier (TIA). Two optical switches are placed before the signal and LO input ports of the hybrid to enable calibration of the shot-noise unit (SNU).

### 3. Real-time CV-QKD Protocol

CV-QKD allows the two involved parties, Alice and Bob, to establish a shared secret key according to a defined protocol. In our system, we implement the Gaussian-modulated (GM), prepare-and-measure, no-switching protocol [40], which enables real-time operation. The security proof enforced in this work is based on the comprehensive review paper [41]. The protocol consists of calibration, transmission, and post-processing steps, executed as a series of automated runs. The generated key is stored in a buffer and managed by a Key Management System (KMS), in our case KEEQuant’s KMS1, which can forward keys on a network level to provide quantum-secure communication [42]. One protocol shot, i.e. a single run, consists of the following steps:

1. **System calibration.** Prior to each quantum exchange, the system is calibrated. This includes tuning of hardware components (e.g., laser power stabilization, IQ modulator biasing) and, crucially, calibration of the shot noise unit (SNU), which serves as the reference for the entire protocol. SNU calibration is performed using the standard two-step approach [41], where one first measures the electronic noise of the receiver,  $N_{el}$ , and then the total noise with no optical input (only LO),  $N_{nosig}$ . The SNU is then defined as

$$N_{\text{shot noise}} = N_{\text{nosig}} - N_{el}. \quad (1)$$

2. **State exchange.** Alice prepares Gaussian-modulated coherent states whose quadratures satisfy  $p, q \sim \mathcal{N}(0, V_{mod})$ . The state is sent through the quantum channel and measured by Bob. The end-to-end data flow is described in detail in Section 4.
3. **Parameter estimation.** To assess whether the parties can establish a secure key, the channel parameters (transmittance  $T$  and excess noise  $\xi$ ) are estimated. To do this, Alice reveals a randomly selected subset of her transmitted quantum symbols. Bob uses these to compute the covariance matrix  $\Gamma_{AB}$  and from  $T$  and  $\xi$ . The asymptotic secret key fraction (SKF) is then given by the Devetak-Winter Formula [41]:

$$\text{SKF} = (1 - \nu)(1 - \text{FER}) (\beta I_{AB} - \chi_{BE}), \quad (2)$$

where  $I_{AB}$  is the mutual information between Alice and Bob;  $\chi_{BE}$  is the Holevo bound in the reverse reconciliation scheme (in the case of individual attacks, it is substituted by the classical information  $I_{EB}$ ) [43];  $\beta$  is the reconciliation efficiency; FER is the frame error rate; and  $\nu$  is the fraction of disclosed symbols for parameter estimation. If  $\text{SKF} > 0$ , the protocol proceeds; otherwise, it resets to the first step. We assume a Gaussian attack, since it is proven to be optimal in both individual and collective attacks [44]. Under this assumption we retrieve  $I_{AB}$  and  $\chi_{BE}$  (or  $I_{EB}$ ) via  $T$  and  $\xi$  [41, 43]. We assume the trusted-detector scenario; therefore, the receiver noise  $\xi_{rec}$  and transmittance  $T_{rec}$  are excluded from the calculation of the Holevo information. Additionally, the system optimizes the modulation variance  $V_{mod}$  based on the estimated channel parameters to maximize the expected key rate for the next quantum exchange.

4. **Information reconciliation.** To convert the measured continuous variables into a bit string, we employ Multi-Dimensional Reconciliation (MDR) [45], which maximizes performance at low SNR, in conjunction with Low-Density Parity-Check (LDPC) codes [46], which achieve efficiencies close to the Shannon capacity.
5. **Confirmation.** A 32-bit cyclic redundancy check (CRC32) is performed between Alice and Bob to confirm they hold the same key.

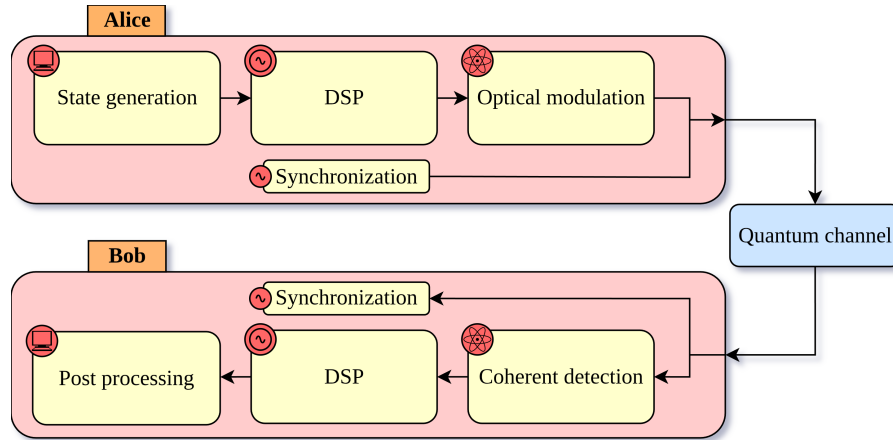


Fig. 4. Diagram illustrating the signal flow in the CV-QKD protocol.

6. **Privacy amplification.** The reconciled keys undergo randomness extraction using a function chosen at random from a family of 2-universal hash function, eliminating any residual information potentially available to an eavesdropper about the final key [47].

All communication between, Alice and Bob in the steps above is done using cryptographic authentication on the classical public channel. The key material used for that is renewed after each shot and is directly obtained from the protocol's key buffers.

#### 4. End-to-end Signal Flow

The exchange of quantum states corresponds to transmission and measurement of Gaussian-modulated quadrature values. To realize this process, digital signals are mapped onto quantum states, transmitted, and then recovered through a series of processing stages. The end-to-end signal flow is illustrated in the flowchart shown in Fig. 4.

The relevant steps of the pipeline are the following:

- **State generation:** The signal is generated digitally using a Pseudo-Random Number Generator (PRNG), which produces two independent series of Gaussian-distributed symbols corresponding to the two optical quadratures.
- **Alice DSP:** The quadrature samples undergo digital upsampling and pulse shaping, confining the spectral content within the available bandwidth. Furthermore, a digital pre-emphasis filter is employed to compensate for the non-flat frequency response of the electrical TX path. To facilitate carrier recovery, the quantum signal is multiplexed with a pilot tone.
- **Optical modulation:** The digital waveform is converted into analog driving voltages for the IQ modulator by means of a DAC. The modulator is biased via Thermo-Optical Phase Shifters (TOPS) to ensure optimal performance. Specifically, the  $I$  and  $Q$  branches are biased at their minima to suppress the carrier, while the relative phase is stabilized at  $90^\circ$ . Following modulation, the optical power is monitored via a photodiode. The signal is subsequently attenuated using a VOA to reach the target modulation variance.
- **Synchronization:** The LO is frequency-stabilized with respect to the signal carrier by means of a pilot tone processed within a proportional–integral–derivative (PID) control

loop. Clock synchronization is achieved through a dedicated synchronization pilot tone, which is used to estimate and compensate for both clock offsets and frequency drifts.

- **Coherent detection:** At the receiver, the incoming quantum signal interferes with a LO in a dual-polarization 90° optical hybrid. The resulting optical outputs are detected by a dual-polarization balanced receiver and digitized by an ADC.
- **Bob DSP:** An equalization filter is implemented to compensate for the frequency response of the receiver. Specifically, a digital Finite Impulse Response (FIR) filter is derived by inverting the experimentally measured transfer function of the receiver. Phase and polarization state recovery are performed using the pilot tone as a reference.

The final output of this processing chain consists of the received digital quadrature values, which serve as the data for the subsequent steps of the QKD protocol.

## 5. Results

To evaluate the performance of the CV-QKD system, two separate tests were carried out. In the first test, the system was operated over optical fibers with a total length of 26, 52, 77 and 102 km. In the second test, optical channels with different length were emulated by introducing additional attenuation using a VOA, in order to assess the system performance over increasing channel loss and establish the maximum achievable reach. The realized real-time protocol assumes trusted detector, individual attacks and operates in the asymptotic regime. The number of exchanged quantum symbols per shot is  $2^{21}$ .

### 5.1. Real-time CV-QKD Analysis

In the CV-QKD literature, the reference metric used to evaluate the performance of a CV-QKD system is the secret key rate, which characterizes the key-generation process over time. Previous implementations used an idealized metric that accounted only for the time of the quantum symbols exchange. We will refer to this rate as quantum states exchange key rate ( $\text{SKR}_{\text{qse}}$ ), given by:

$$\text{SKR}_{\text{qse}} = \frac{n_{\text{key}}}{t_{\text{sym}}} = p_{\text{suc}} \cdot \text{SKF} \cdot f_{\text{sym}} \quad (3)$$

Where SKF is the secret key fraction,  $f_{\text{sym}}$  is the symbol rate,  $n_{\text{key}}$  is the number of established secret key bits, and  $t_{\text{sym}}$  the time necessary for exchanging the quantum symbols. The shot success rate  $p_{\text{suc}}$  represents the protocol failure factors associated with real-time operation, such as synchronization, parameter estimation, post-processing failures etc.; therefore, it is neglected in offline CV-QKD demonstrations. The reason this metric was commonly adopted lies in typical offline post-processing, which only allows one to infer a rate for the system, since the key is not generated in real time. To do this, the adopted standard is to consider the fundamental time-limiting characteristic of the offline process: the quantum states exchange. When accounting for the real-time nature of the protocol, this commonly used metric gives only limited information, since it does not reflect the protocol duration. For this motivation, we suggest to adopt the real-time key rate ( $\text{SKR}_{\text{rt}}$ ), accounting for the entire protocol, including the duration of calibration, post-processing, and other overheads. This metric represents the effective key generated over time that an end-user could access. We define it as follows:

$$\text{SKR}_{\text{rt}} = \frac{n_{\text{key}}}{t} = p_{\text{suc}} \cdot \text{SKF} \cdot f_{\text{shot}} \quad (4)$$

Here,  $n_{\text{key}}$  is the number of established secret key bits,  $t_{\text{sym}}$  is the total measurement time, and  $f_{\text{shot}}$  represents the shot rate, which in addition to the symbols exchange, incorporates calibration,

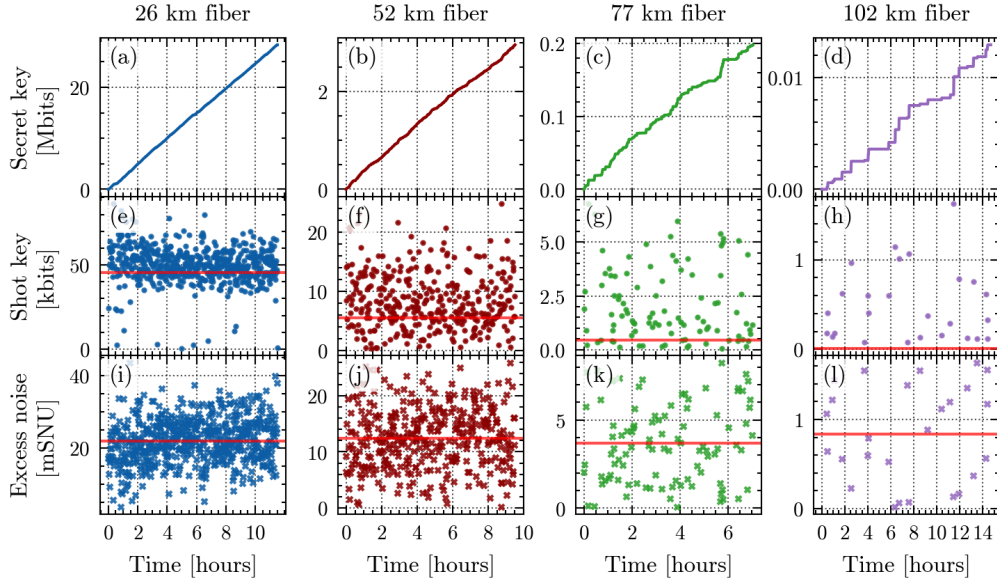


Fig. 5. Characterization over time of the CV-QKD system featuring the chip-scale transmitter over optical fibers of 26, 52, 77, and 102 km. The plots show the real-time operation of the protocol, displaying: (a)–(d) the total established secret key; (e)–(h) the key length of the successful shots; and (i)–(l) the corresponding excess noise. The red lines in (e)–(l) for shot key length and excess noise represent their average values. The average shot key length also accounts for the unsuccessful shots.

DSP, synchronization and post-processing time. The two rates are related by:

$$\text{SKR}_{\text{qse}} = \text{SKR}_{\text{rt}} (1 + x), \quad x = \frac{t - t_{\text{sym}}}{t}. \quad (5)$$

They are comparable only when  $t \approx t_{\text{sym}}$ , which represents an ideal scenario, since post-processing remains the primary resource-intensive step.

## 5.2. Performance Evaluation over Optical Fiber

The system performance was evaluated over fiber lengths of 26, 52, 77 and 102 km. Measurements were carried out in the lab by means of fiber spools. The corresponding experiments ran continuously for 690, 571, 423, and 881 minutes during which a total of 624, 537, 444 and 1106 shots were acquired, respectively. The characterizing metrics of the CV-QKD system are summarized Table 1.

Fig. 5 displays the real-time QKD system performance over the employed optical fibers. The plots showcase the total secret key generated over time, and the underlying single shots, with the corresponding values of generated secret key and excess noise. As shown in Fig. 5, the key generation process guaranteed constant key updates over the measurement period for all evaluated distances, allowing key-refreshing for real-time encryption. For the 26 km and 52 km optical links, key updates were frequent even over short time intervals, ensuring high reliability and low key-update latency. The overall shot-success probabilities for these measurements were 90.5% and 65.6%, respectively, with the few failed shots distributed evenly among synchronization, parameter estimation, and error correction issues. Increasing the channel length to 77 km and 102 km decreased the success rates to 22% and 2%, respectively, thereby reducing the frequency of key updates. The underlying reason for this reduction was a lower probability of successful

parameter estimation, as longer channels impose stricter excess-noise constraints. Over the full measurement periods, the system generated 28.32 Mbits, 2.96 Mbits, 198 kbits, and 13 kbit of secret key material, corresponding to real-time key rates of 721, 91, 8.1 and 0.2 bit/s. The system achieved a quantum states exchange key rate of 3.4 Mbit/s, 410 kbit/s, 33 kbit/s, and 1 kbit/s. Regarding noise performance, the measured excess noise of the successful shots (referred to the channel output) varied from 22 to 0.8 mSNU when increasing the fiber length. The system operated with increasing modulation variances from 4.2 to 13.2 SNU, automatically set during operation for key rate maximization. The overall channel losses were 5.76, 10.60, 15.65 and 20.80 dB. Concerning the trusted receiver, the measured electronic noise was 0.14 SNU and the transmittance (i.e. efficiency) was 48%.

Table 1. Evaluation of CV-QKD system parameters over optical fibers of varying lengths. The channel metrics consider the successful shots. The reported parameters, from left to right, include: fiber length ( $L_{ch}$ ), real-time key rate ( $\text{SKR}_{rt}$ ), quantum states exchange key rate ( $\text{SKR}_{qse}$ ), excess noise and transmittance of channel and receiver ( $\xi_{ch}, T_{ch}, \xi_{rec}, T_{rec}$ ), modulation variance ( $V_{mod}$ ), reconciliation efficiency ( $\beta$ ), frame error rate (FER), and shot success rate ( $p_{suc}$ ).

$L_{ch}$ [km]	$\text{SKR}_{rt}$ [bit/s]	$\text{SKR}_{qse}$ [Mbit/s]	$\xi_{ch}$ [mSNU]	$T_{ch}$ [%]	$\xi_{rec}$ [mSNU]	$T_{rec}$ [%]	$V_{mod}$ [%]	$\beta$ [SNU]	FER [%]	$p_{suc}$ [%]
26	721	3.38	22.0	26.5	141	48.0	4.2	91.2	0.07	90.5
52	90.5	0.41	12.4	8.7	144	48.0	4.4	92.7	4.1	65.6
77	8.1	0.033	3.7	2.7	144	48.0	7.8	93.7	18.6	21.6
102	0.2	0.0009	0.8	0.8	144	48.0	13.2	94.5	31.6	2.4

Notably, accounting for a live operation, the real-time key rate is about four orders of magnitude lower than the quantum states exchange key rate, because post-processing takes most of the system runtime. Therefore, the quantum states exchange key rate alone provides limited insight for real deployment scenarios, as it does not capture the main bottleneck of CV-QKD systems, which lies in the post-processing rate rather than the symbol rate. For this reason, the real-time key rate, is a more informative metric for assessing CV-QKD system performance in practical use cases, as it reflects all aspects of the protocol and provides a more appropriate reference for real-time encryption applications.

Compared to previous works which attempted to integrate CV-QKD systems on the transmitter side [29, 30, 35–39], the main components of the CV-QKD transmitter—laser and IQ modulator—have been individually integrated on PICs. However, no prior work has demonstrated a complete chip-scale system. Moreover, these demonstrations lack real-time operation, a key limitation that we have overcome to bring QKD to operation in real environments. The comparison of secret key fractions across previously reported systems is illustrated in Fig. 6, with detailed performance metrics summarized in Table 2. The plot shows improvements over previous studies in the 5 dB range of channel loss, and performance consistent with prior work in the 10 dB range. Furthermore, we extend the typical reach reported in earlier studies with a 77 km channel, and notably, we set a record for the longest distance achieved by a CV-QKD system using chip-scale components, covering a distance of 102 km with corresponding attenuation of 20.8 dB. These results demonstrate that the fully chip-scale transmitter delivers excellent performance despite full hardware miniaturization. The system supports typical metropolitan links in a point-to-point architecture and can extend to long-distance coverage when combined with trusted nodes, paving

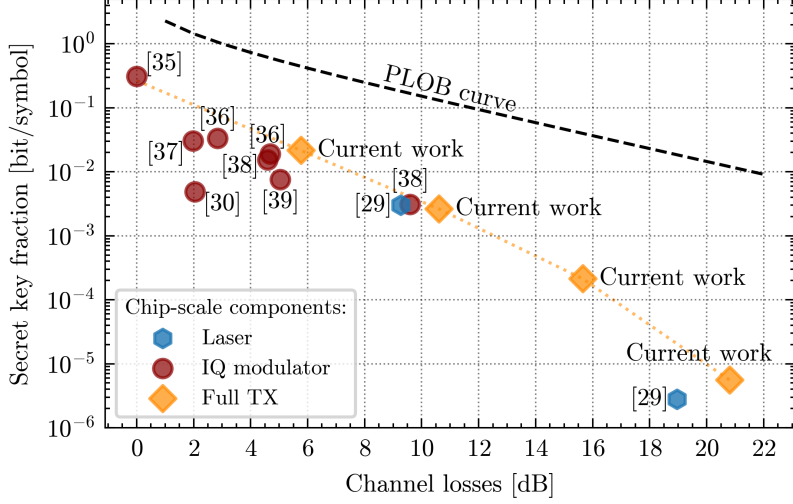


Fig. 6. Comparison of experimental secret key rates for CV-QKD transmitters employing various chip-scale components (detailed in the legend) versus channel losses. The dotted orange line guides the eye for comparison with previous results. The dashed black line marks the PLOB bound (Pirandola-Laurenza-Ottaviani-Banchi), the fundamental limit for the secret key rate [48].

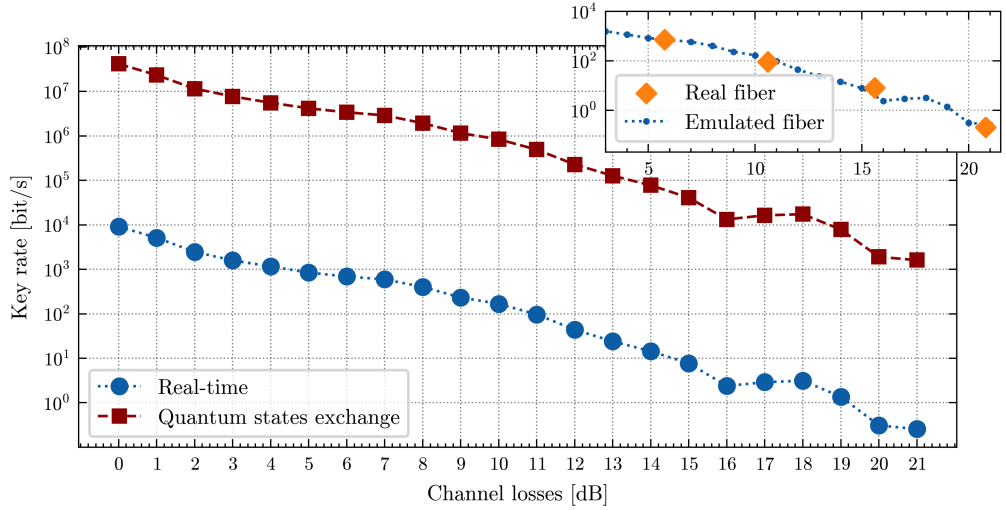
the way for practical, scalable implementations of CV-QKD networks.

### 5.3. Performance Evaluation over Emulated Optical Fiber with Variable Loss

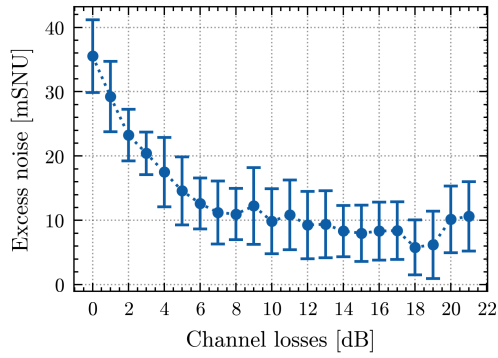
The second measurement concerns the evaluation of the system performance over a quantum channel with controlled channel losses, implemented via signal attenuation using a VOA. The experiment consisted of a total of 1872 shots acquired over 29 hours, while sweeping the channel losses from 0 dB (back-to-back configuration) up to 21 dB. These values correspond to emulated fiber lengths ranging from 0 to 105 km, assuming typical fiber attenuation at 1550 nm of 0.2 dB/km. The results are reported in Fig. 7.

The system operated up to 21 dB of channel loss, achieving a real-time key rate ranging from 9.1 kbit/s at 0 dB loss to 0.3 bit/s at 21 dB loss. In terms of quantum states exchange key rate, this corresponds to values between 41.6 Mbit/s and 1.6 kbit/s. These results are shown in Fig. 7a. Observing the channel excess noise including successful and unsuccessful shots, as shown in Fig. 7b, we notice a decrease with increasing channel attenuation from 36 mSNU to 10 mSNU. This behavior suggests that the dominant noise contribution originates from the transmitter, which includes the laser (phase noise, RIN) and the IQ modulator (extinction ratio, compression, drivers). Interestingly, we observe the excess noise reaching a plateau when approaching high channel losses, degrading the performance. Phase recovery, achieved via a pilot tone, is the main contributor to this behavior, in fact the pilot is subjected to the same attenuation of the symbols, both when  $V_{\text{mod}}$  is set and during propagation through the channel. As shown in Fig. 7c, the symbols signal-to-noise ratio (SNR) degrades by 17 dB over evaluated losses range, the same happens to the pilot tone. At high channel losses, the pilot-tone SNR degrades to the point of affecting phase-recovery accuracy, resulting in additional artificial excess noise, which explains the reduced shot success rate, given the tighter key-generation requirements for the channels parameters.

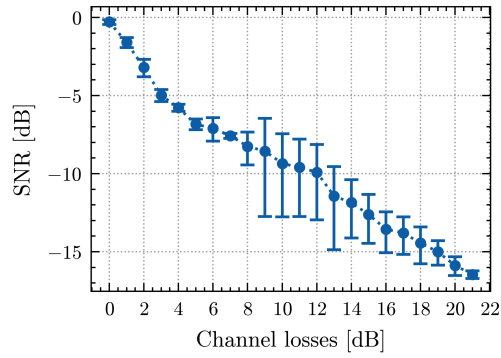
When we compare the experimental results obtained over real fiber with those from the emulated optical channel, as shown in the top right region of Fig. 7a, we observe consistency in the key



(a)



(b)



(c)

Fig. 7. CV-QKD system characterization over quantum channels with variable losses. The plots represent relevant metrics vs. channel losses, specifically: (a) shows real-time and quantum states exchange key rate, as well as a close-up for comparison of real-time key rate over emulated and real fiber. (b) and (c) show average and standard deviation of channel excess noise and quantum symbols SNR at the receiver. These values includes the unsuccessful shots, excluding outliers.

Table 2. Comparative table of CV-QKD experimental demonstrations featuring transmitter chip-scale components evaluated over optical fibers. The table lists references, specific chip-scale components, real-time and quantum states exchange key rate, secret key fraction, symbol rate and channel length.

Reference	Chip-scale modules	$\text{SKR}_{\text{rt}}$ [bit/s]	$\text{SKR}_{\text{qse}}$ [bit/s]	SKF [mbit/sym]	$f_{\text{sym}}$ [MBaud]	$L_{\text{ch}}$ [km]	
[29]	Laser	None	750k	3.0	250	50	
			700	0.003		100	
[30]	IQ mod.	None	78k	4.9	16	11	
[35]	IQ mod.	None	250k	313	0.8	0.002	
[36]	IQ mod.	None	534M	33.4	16000	10	
			246M	15.4		20	
[37]	IQ mod.	None	1.21G	30.3	40000	10	
[38]	IQ mod.	None	31.1M	19.1	1625	25.8	
			5.05M	3.1		50.4	
[39]	IQ mod.	None	1.9M	7.6	250	25.2	
			721	3.38M		21.6	26
			90.5	410k		2.6	52
Current work	Full TX		8.1	33k	156.25	77	
			0.2	871		0.006	102

rate datapoints, suggesting that the behaviour of the optical link can be effectively emulated by VOA attenuation. Basing on this observation we can realistically set the maximum system reach to 21 dB of channel losses, confirming the measurements over a 102 km optical fiber.

## 6. Conclusions

In this work, we demonstrated the first CV-QKD system featuring a complete chip-scale transmitter. The presented TX module leverages telecom-grade chip-scale IQ modulator and laser, adapted for CV-QKD applications. This miniaturized design enables a significant reduction in footprint, cost and manufacturing scalability, allowing a complete CV-QKD transmitter to be implemented in currently precluded form factors, such as pluggables or PCIe cards.

The system incorporating this module generates secure keys in real time at rates up to 9.1 kbit/s and supports optical links with losses up to 21 dB, with validated secret-key generation over a 102 km channel. This performance enables secure communication over typical metropolitan links and can extend to longer distances when combined with trusted nodes, providing key rates compatible with real-time AES encryption. These results represent a significant step towards practical, compact, and deployable quantum-secured communication systems, paving the way for broader applications in finance, healthcare, and beyond.

Future research will focus on extending this level of miniaturization to the receiver, incorporating

chip-scale laser and integrated coherent detector, to demonstrate a complete scalable CV-QKD system. Additional efforts will target DSP and post-processing optimization to further increase system reach and real-time key rates.

**Funding:** Funded by the European Union as part of the projects QuNEST and SEQRET (Grant Agreements: 101120422, 101091591). Views and opinions expressed are, however, those of the author(s) only and do not necessarily reflect those of the European Union or REA. Neither the European Union nor the granting authority can be held responsible for them.



**Acknowledgments:** The authors thank Laurent Schmalen and Frank Volland for their valuable comments and for reviewing the manuscript, and the whole KEEQuant team for insightful discussions and support.

**Data availability:** Data underlying the results presented in this paper are not publicly available at this time but may be obtained from the authors upon reasonable request.

## References

1. P. W. Shor, "Algorithms for quantum computation: Discrete logarithms and factoring," in *Proceedings of the 35th Annual Symposium on Foundations of Computer Science (FOCS)*, (1994), pp. 124–134.
2. R. L. Rivest, A. Shamir, and L. Adleman, "A method for obtaining digital signatures and public-key cryptosystems," *Commun. ACM* **21**, 120–126 (1978).
3. W. Diffie and M. Hellman, "New directions in cryptography," *IEEE Trans. on Inf. Theory* **22**, 644–654 (1976).
4. C. H. Bennett and G. Brassard, "Quantum cryptography: Public key distribution and coin tossing," in *Proceedings of IEEE International Conference on Computers, Systems and Signal Processing*, (1984), pp. 175–179.
5. A. K. Ekert, "Quantum cryptography based on bell's theorem," *Phys. Rev. Lett.* **67**, 661–663 (1991).
6. C. H. Bennett, "Quantum cryptography using any two nonorthogonal states," *Phys. Rev. Lett.* **68**, 3121–3124 (1992).
7. H.-K. Lo, M. Curty, and B. Qi, "Measurement-device-independent quantum key distribution," *Phys. Rev. Lett.* **108**, 130503 (2012).
8. T. C. Ralph, "Continuous variable quantum cryptography," *Phys. Rev. A* **61** (1999).
9. S. Ren, S. Yang, A. Wonfor, *et al.*, "Demonstration of high-speed and low-complexity continuous variable quantum key distribution system with local local oscillator," *Sci. Reports* **11** (2021).
10. T. Wang, P. Huang, Y. Zhou, *et al.*, "High key rate continuous-variable quantum key distribution with a real local oscillator," *Opt. express* **26** **3**, 2794–2806 (2018).
11. H. Wang, Y. Pi, W. Huang, *et al.*, "High-speed gaussian-modulated continuous-variable quantum key distribution with a local local oscillator based on pilot-tone-assisted phase compensation," *Opt. express* **28** **22**, 32882–32893 (2020).
12. H. Wang, Y. Li, Y. Pi, *et al.*, "Sub-Gbps key rate four-state continuous-variable quantum key distribution within metropolitan area," *Commun. Phys.* **5** (2021).
13. T. Wang, P. Huang, L. Li, *et al.*, "High key rate continuous-variable quantum key distribution using telecom optical components," *New J. Phys.* **26** (2024).
14. A. A. E. Hajomer, I. Derkach, N. Jain, *et al.*, "Long-distance continuous-variable quantum key distribution over 100-km fiber with local local oscillator," *Sci. Adv.* **10** (2023).
15. Y. Zhang, Z. Chen, S. Pirandola, *et al.*, "Long-distance continuous-variable quantum key distribution over 202.81 km of fiber," *Phys. review letters* **125** **1**, 010502 (2020).
16. D. Huang, P. Huang, D. Lin, and G. Zeng, "Long-distance continuous-variable quantum key distribution by controlling excess noise," *Sci. Reports* **6**, 19201 (2016).
17. D. Qi, X. Wang, J. Ma, *et al.*, "Long distance local local oscillator continuous variable quantum key distribution with digital signal processing," *arXiv preprint arXiv:2508.02392* (2025).
18. A. A. E. Hajomer, I. Derkach, V. C. Usenko, *et al.*, "Coexistence of continuous-variable quantum key distribution and classical data over 120 km fiber," *Phys. review letters* **135** **17**, 170804 (2025).
19. T. Kawakami, H. Kawahara, T. Okamura, and W. Maeda, "Coexistence demonstration and wavelength dependency analysis of s-band CV-QKD signal with fully loaded c+l-band DWDM signals," *Entropy* **27** (2025).
20. J. Geng, G.-J. Fan-Yuan, S. Wang, *et al.*, "Coexistence of quantum key distribution and optical transport network based on standard single-mode fiber at high launch power," *Opt. letters* **46** **11**, 2573–2576 (2021).

21. X. Wang, J. Wang, Y. Chen, *et al.*, “Field trial of  $7 \times 89\lambda \times 256$  Gb/s c-band classical / CVQKD co-existence transmission over 7-core fiber,” 2023 Asia Commun. Photonics Conf. Int. Photonics Optoelectron. Meet. (ACP/POEM) pp. 1–4 (2023).
22. Y. Shao, Z. Shen, Y. Xu, *et al.*, “Integration of classical communication and quantum key distribution using frequency division multiplexing,” *Chin. Opt. Lett.* (2025).
23. S. Kleis, J. Steinmayer, R. H. Derksen, and C. G. Schaeffer, “Experimental investigation of heterodyne quantum key distribution in the s-band or l-band embedded in a commercial c-band DWDM system,” *Opt. express* **27** **12**, 16540–16549 (2019).
24. P. Gavignet, F. Mondain, E. Pincemin, *et al.*, “Co-propagation of 6 Tb/s (60\*100Gb/s) DWDM & QKD channels with 17 dBm aggregated WDM power over 50 km standard single mode fiber,” 2023 Opt. Fiber Commun. Conf. Exhib. (OFC) pp. 1–3 (2023).
25. A. Melgar, M. Iqbal, M. S. Moreolo, *et al.*, “Coexistence of commercial CV-QKD in FOADM-based metro networks with full or partial c-band utilization,” 2025 Opt. Fiber Commun. Conf. Exhib. (OFC) pp. 1–3 (2025).
26. T. A. Eriksson, B. J. Puttnam, G. Rademacher, *et al.*, “Crosstalk impact on continuous variable quantum key distribution in multicore fiber transmission,” *IEEE Photonics Technol. Lett.* **31**, 467–470 (2019).
27. T. Kawakami, H. Kawahara, T. Okamura, *et al.*, “No-guard-band integration of digital coherent CV-QKD system into 400 Gbit/s 75 GHz grid DWDM systems,” 2024 Opt. Fiber Commun. Conf. Exhib. (OFC) pp. 1–3 (2024).
28. F. Honz, F. Prawits, O. Alia, *et al.*, “First demonstration of  $25\lambda \times 10$  Gb/s c+l band classical / DV-QKD co-existence over single bidirectional fiber link,” *J. Light. Technol.* **41**, 3587–3593 (2022).
29. L. Li, T. Wang, X. Li *et al.*, “Continuous-variable quantum key distribution with on-chip light sources,” *Photonics Res.* **11**, 504–516 (2023).
30. J. Aldama, S. Sarmiento, L. T. Vidarte *et al.*, “Integrated InP-based transmitter for continuous-variable quantum key distribution,” *Opt. Express* **33**, 8139–8149 (2025).
31. Y. Bian, Y. Li, X. Xu *et al.*, “Highly stable power control for chip-based continuous-variable quantum key distribution system,” *Opt. Lett.* **49**, 2521–2524 (2024).
32. Y. Piétri, L. T. Vidarte, M. Schiavon *et al.*, “Experimental demonstration of continuous-variable quantum key distribution with a silicon photonics integrated receiver,” *Opt. Quantum* **2**, 428–437 (2024).
33. Y. Bian, Y. Pan, X. Xu *et al.*, “Continuous-variable quantum key distribution over 28.6 km fiber with an integrated silicon photonic receiver chip,” *Appl. Phys. Lett.* **124** (2024).
34. A. A. Hajomer, C. Bruynsteen, I. Derkach *et al.*, “Continuous-variable quantum key distribution at 10 Gbaud using an integrated photonic-electronic receiver,” *Optica* **11**, 1197–1204 (2024).
35. J. Zhang, J. Y. Haw, H. Cai, *et al.*, “An integrated silicon photonic chip platform for continuous-variable quantum key distribution,” *Nat. Photonics* **13**, 839 – 842 (2019).
36. A. A. E. Hajomer, A. Bomhals, C. Bruynsteen, *et al.*, “Chip-based 16 Gbaud continuous-variable quantum key distribution,” arXiv preprint arXiv:2504.09308 (2025).
37. A. Q. Ng, F. Kanitschar, G. Zhang, and C. Wang, “Gigabit-rate quantum key distribution on integrated photonic chips,” arXiv preprint arXiv:2504.08298 (2025).
38. S. Liu, Y. Jia, Y. Shi, *et al.*, “Continuous-variable quantum key distribution over 50.4 km fiber using integrated silicon photonic transmitter and receiver,” arXiv preprint arXiv:2508.08722 (2025).
39. D. Fatkhiev, J. d. Reis Frázao, A. H. Derkani, *et al.*, “Compact continuous-variable quantum key distribution system employing monolithically integrated silicon photonic transceiver,” in *2025 European Conference on Optical Communications (ECOC)*, (2025), pp. 1–4.
40. C. Weedbrook, A. M. Lance, W. P. Bowen, *et al.*, “Quantum cryptography without switching,” *Phys. Rev. Lett.* **93**, 170504 (2004).
41. F. Laudenbach, C. Pacher, M. Pivoluska, *et al.*, “Continuous-variable quantum key distribution with gaussian modulation – the theory of practical implementations,” *Adv. Quantum Technol.* **1**, 1800011 (2018).
42. P. Horoschenkoff, J. Henrich, R. Böhn, *et al.*, “DemoQuanDT: a carrier-grade QKD network,” *J. Opt. Commun. Netw.* **17**, 743–756 (2025).
43. V. Scarani, H. Bechmann-Pasquinucci, N. J. Cerf, *et al.*, “The security of practical quantum key distribution,” *Rev. Mod. Phys.* **81**, 1301–1350 (2009).
44. R. García-Patrón and N. J. Cerf, “Unconditional optimality of gaussian attacks against continuous-variable quantum key distribution,” *Phys. Rev. Lett.* **97**, 190503 (2006).
45. A. Leverrier, R. Alléaume, J. Boutros, *et al.*, “Multidimensional reconciliation for a continuous-variable quantum key distribution,” *Phys. Rev. A* **77**, 042325 (2008).
46. R. Gallager, “Low-density parity-check codes,” *IRE Trans. on Inf. Theory* **8**, 21–28 (1962).
47. C. H. Bennett, G. Brassard, and J.-M. Robert, “Privacy amplification by public discussion,” *SIAM J. Comput.* **17**, 210–229 (1988).
48. S. Pirandola, R. Laurenza, C. Ottaviani, and L. Banchi, “Fundamental limits of repeaterless quantum communications,” *Nat. Commun.* **8**, 15043 (2017).